ACS OMEGA

http://pubs.acs.org/journal/acsodf

Article

# Facile and Sustainable Synthesis of ZnO Nanoparticles: Effect of Gelling Agents on ZnO Shapes and Their Photocatalytic Performance

Loubna El Faroudi, Latifa Saadi, Abdellatif Barakat, Mohammed Mansori, Karima Abdelouahdi,* and Abderrahim Solhy

Cite This: *ACS Omega* 2023, 8, 24952−24963

Read Online

ACCESS | Metrics & More | Article Recommendations | Supporting Information

**ABSTRACT:** The present work involves investigating an unexplored soft-chemical method for synthesizing nanostructured ZnO through biopolymer gelation. Our objective was to exploit (i) the difference in the gelation mechanism of four tested biopolymers, namely, alginate, chitosan, carboxymethylcellulose (CMC), and pectin and (ii) numerous experimental parameters that govern this process in order to allow the control of the growth of nanostructured ZnO, with a view to using the prepared oxides as photocatalysts for the oxidation of the Orange G dye. So, the effect of biopolymer's nature on the microstructural, morphological, and textural properties was examined by thermogravimetric analysis (TGA), X-ray diffraction (XRD), Fourier transform infrared (FTIR) spectroscopy, field-emission gun-scanning electron microscopy-high resolution (FEG-SEM) with energy-dispersive spectrometry (SEM-EDS), ultraviolet−visible (UV−vis) spectroscopy, and $N_2$ adsorption/desorption. As-prepared oxides were crystallized in a hexagonal wurtzite structure, with a clear difference in their morphologies. The sample prepared by using chitosan has a specific surface area of around 36.8 $m^2/g$ in the form of aggregated and agglomerated nanostructured minirods and thus shows the best photocatalytic performance with 99.3% degradation of the Orange G dye in 180 min.

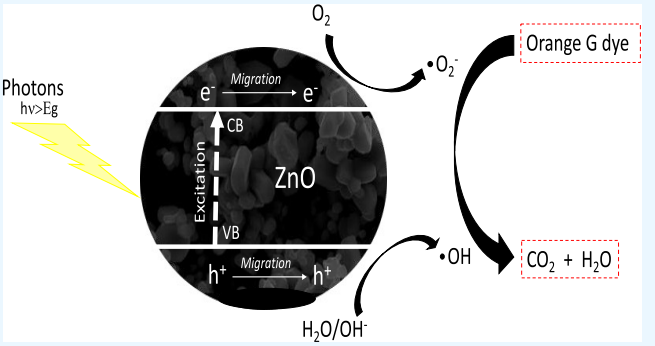


## INTRODUCTION

ZnO is a very promising material offering or giving high-tech applications and key to the development of Green Technologies.[1] It is one of the few multifunctional materials thanks to its many interesting physical, chemical, and optoelectronic properties, which confer it to be a material used in various fields of applications, such as solar cells,[2] gas sensors,[3] depollution (water and air) by photocatalytic effect,[4] etc. This oxide has already found potential industrial applications, such as rubber,[5] paints,[6] animal feed,[7] cosmetics, and pharmaceuticals.[8−10] ZnO has very good thermal and chemical stability, is nontoxic and biocompatible,[11−13] and the raw materials necessary for its production are abundant.[14]

Under the effect of light excitation, ZnO helps to accelerate the oxidation reaction by increasing considerably its advance rate to lead to a complete mineralization of the organic contaminants, such as pesticides,[15] dyes,[16,17] pharmaceutical compounds,[18] volatile organic compounds,[19] or even microbiological compounds (bacteria, virus, fungi, etc.).[20,21] Furthermore, dyes are widely used in various industries, including textiles and food, but their widespread use has also led to a growing environmental problem. Dyes can also have negative impacts on the environment and human health due to their toxicity and persistent nature.[22] The Orange G dye was selected as one of the widely used dyes in various industries; it can also cause serious ecological problems, such as water pollution and the inhibition of the growth of aquatic organisms. By using the Orange G dye as a model pollutant, researchers can study the efficacy of various photocatalytic materials and technologies for the degradation of this pollutant, and the results can be applied to other similar pollutants in the environment.[23,24]

Heterogeneous photocatalysis is a very successful strategy for degrading and mineralizing organic dyes. It has various advantages, such as high removal efficiency, low cost, and low power requirements. Besides, this process allows the total mineralization of emerging contaminants avoiding the release of secondary pollutants.[25,26] The photocatalytic efficiency of ZnO is mainly related to the synthesis processes,[27,28] and among

Received: March 5, 2023
Accepted: May 16, 2023
Published: July 3, 2023

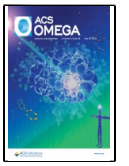

other things, its nanostructuring (the size and shape of the nanoparticles (NPs)).[29] It depends essentially on the degree of perfection of the crystal lattice: vacancies, atoms in interstitial positions, and antisites (a "Zn" atom involving an "O" lattice site or vice versa).[30] Indeed, the main obstacle for its use in photocatalysis is its high recombination rate of electron−hole pairs[31] and its high band gap energy (about 3.37 eV).[32]

Many methods for ZnO NP synthesis have been reported in wet chemistry, such as the sol−gel method,[33] precipitation,[34] and hydrothermal method.[35] Recently, many applications needed nanostructured ZnO.[9] Cost-effective design synthesis of ZnO by the deep coating method has also been studied to reveal the degradation of DO26 under light illumination.[36] Besides, ZnO nanocrystals have demonstrated superior efficiency in degrading Reactive Orange 4 under ultraviolet (UV)-A light when compared to commercial ZnO and $TiO_2$ (P25).[37] By using proper synthesis processes and controlling the local growth kinetics and temperature as well as the chemical composition of the starting precursors, including postsynthesis treatment, a wide range of nanostructured ZnO with different shapes, sizes, and very different properties can be easily synthesized.[38] However, the synthesis of ZnO NPs remains a challenge.[39]

Eco-design and emerging bio-based methods for synthesizing nanomaterials, especially oxides, represent promising avenues to overcome the obstacles related to the control of nucleation and growth, including downstream processing of these materials by conventional manufacturing methods and then making them more efficient and cleaner.[40] For this reason, several research studies had been done to synthesize ZnO NPs by using various sources like bacteria, fungus, algae, plants, biopolymers, and others.[41−47] In this context, our team developed a method derived from "*chimie-douce*" based on the ability of certain biopolymers to gel in the presence of a monovalent (+I), divalent (+II), trivalent (+III), or tetravalent (+IV) metal. Thus, we controlled the nucleation and growth of zirconia, ceria, and titania for catalysis and photocatalysis applications.[40,48,49] So, the present work is a continuation of our strategy undertaken in recent years to develop eco-friendly approaches to the synthesis of nanomaterials for various applications. For this purpose, we compared the gelation process of four polysaccharides, namely, alginate, carboxymethylcellulose (CMC), pectin, and chitosan, to be able to control the nucleation and growth of nanostructured ZnO and then study the influence of the biopolymer structure on the intrinsic properties of this oxide, especially in terms of photocatalytic performance, by measuring the photodegradation of Orange G. Four ZnO samples were prepared with $Zn^{2+}$ cations using the four biopolymers mentioned above. The prepared xerogels were characterized by thermogravimetric analysis (TGA) to determine the calcination temperature to properly crystallize the oxide. A battery of analytical tools was used to characterize the synthesized samples.

## MATERIALS AND METHODS

**Materials and Apparatus.** Nanostructured zinc oxide was synthesized using zinc chloride ($ZnCl_2$, 98.6%) obtained from VWR Chemicals. Sodium alginate, chitosan, and CMC were purchased from Sigma-Aldrich, while pectin powder was purchased from Acros Organics. Sodium hydroxide (NaOH, 99%) was obtained from VWR Chemicals, and acetic acid ($CH_3CO_2H$, 99.8%) was purchased from Sigma-Aldrich. The anionic Orange G was obtained from Merck KGaA. All chemicals were used without further purification.

**Characterization.** TGA was conducted under air in a Labsys Evo apparatus with a 5 °C/min ramp between 25 and 1000 °C. The structural properties of the prepared zinc oxides were determined by X-ray diffraction (XRD) on a Rigaku Smart Lab SE X-ray diffractometer using the Bragg Brentano configuration in the $2\theta$ range of 25−80° and with Cu K$\alpha$ radiation ($\lambda$ = 1.5406 Å). Fourier transform infrared spectroscopy (FTIR) spectra of the prepared samples were measured using KBr in the range of 4000−400 $cm^{-1}$ on a Bruker VERTEX 70. The morphologies of the prepared samples were observed by a JOEL-JSM 7200f field-emission gun-scanning electron microscope (FEG-SEM) equipped with an EDAX energy-dispersive spectroscopy (EDS) microanalysis system. Energy-dispersive spectroscopy was used to study the chemical composition of the as-synthesized samples. The surface charge of the oxides was measured on a Zetasizer (Nano ZS, Malvern Instruments Ltd, 7.12). The gas adsorption data were collected using a Micromeritics FlowSorb III, a surface area analyzer, using $N_2$. Prior to $N_2$ sorption, all samples were degassed at 150 °C overnight. The specific surface areas were determined from the nitrogen adsorption/desorption isotherms (at −196 °C) using the Brunauer−Emmett−Teller (BET) method. UV−visible (UV−vis) spectroscopy measurements were performed for all samples using a UV−vis spectrometer operating in the wavelength range of 300−700 nm.

**Preparation of Porous Nanostructured ZnO.** It should first be noted that the direct gelation synthesis was performed using sodium alginate, CMC, and pectin, while for chitosan, we used two-step gelation. For the direct gelation (Figure S1), a specific weight of zinc chloride was first dissolved in ultrapure water for the preparation of a zinc precursor solution with a concentration of 0.1 M. The gelling agent solution (4% wt) was also prepared by dissolving 4 g of the biopolymer (sodium alginate, CMC, or pectin) in 100 mL of ultrapure water under vigorous stirring at room temperature for 10 h to form a gel (homogeneous viscous solution). The biopolymer's gel was then added dropwise into the solution of the zinc precursor under slow agitation and stirred for 3 h to form hydrogel beads. Those hydrogel beads were washed several times with deionized water, and then they were dried at room temperature overnight to form xerogel beads. Thereafter, those xerogels were calcined under air at 850 °C for 8 h. The heat treatment in this case removes the organic matrix and yields pure zinc oxide. The obtained zinc oxide was crushed manually using a mortar for 10 min. When using chitosan as a gelling agent, the gelation process was achieved in two steps (Figure S2). The chitosan gel (1% wt) was also prepared by dissolving 1 g of chitosan in 100 mL of acetic acid solution (1% v/v) under vigorous stirring at room temperature for 10 h. This chitosan gel was then added dropwise using a syringe with a needle into a NaOH solution (1 M) under slow agitation to form uniform hydrogel beads. After that, the formed beads were placed in the zinc precursor solution (0.1 M) and allowed to stir for 3 h. The postsynthesis treatment was the same as before in order to release the inorganic matrix (ZnO). The various hybrid materials and corresponding oxides are designated as shown in Table 1.

**Photocatalytic Dye Degradation Experiments.** The photocatalytic performance of the prepared samples was tested in pollutant dye photodegradation "Orange G" using UV irradiation in a "Techinstro" type reactor. The photocatalytic experiments were carried out in a 500 mL cylindrical quartz reactor equipped with a closed water circulation system. A 250 W mercury lamp was used as the UV light source. So, 100 mg of


https://doi.org/10.1021/acsomega.3c01491
ACS Omega 2023, 8, 24952−24963

**Table 1. References of the As-Prepared ZnO Samples According to the Used Gelling Agent**

| gelling agent (biopolymer) | xerogel (before calcination) | oxide (after calcination) |
|---|---|---|
| sodium alginate | Zn@Alg-X | ZnO-Alg |
| chitosan | Zn@Chi-X | ZnO-Chi |
| CMC | Zn@CMC-X | ZnO-CMC |
| pectin | Zn@Pec-X | ZnO-Pec |

the photocatalyst was suspended in 100 mL of the Orange G solution. Before irradiation, the suspension was magnetically stirred for 1 h in the dark to ensure uniform dispersion of the photocatalyst and to achieve an adsorption/desorption equilibrium. During all photocatalytic experiments, every 15 min, 3 mL of the suspension was taken, centrifuged, and analyzed by measuring the absorbance at $\lambda_{max}$ = 478 nm using a UV−visible spectrophotometer. The concentration of degraded dye is determined from a calibration curve created previously.

## RESULTS AND DISCUSSION

**Characterization of Hybrid Beads (Xerogels).** *Thermogravimetric Analysis of Hybrid Beads.* It is well known that the calcination temperature influences the structural properties and photocatalytic performance of an oxide. For this, we used TGA to get an idea of the temperature range, where we have to calcine the xerogels in order to be able to release oxides crystallographically pure.

Figure 1 shows the thermal decomposition of Zn@Alg-X, Zn@Chi-X, Zn@CMC-X, and Zn@Pec-X. The thermal

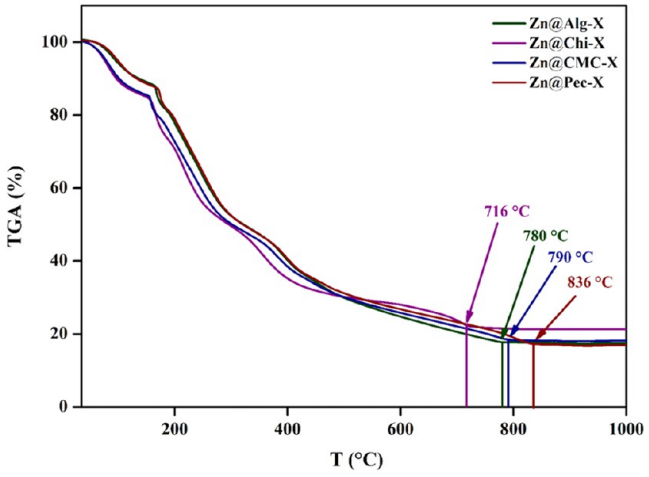


**Figure 1.** TGA of xerogels prepared by polymer gelation with $Zn^{2+}$ cations: alginate (green), chitosan (red), CMC (blue), and pectin (brown).

decomposition of the different samples was almost similar. The first mass loss is observed in the range of 35−165 °C. It is attributed to the dehydration of xerogels (Zn@Alg-X, Zn@Chi-X, Zn@CMC-X, and Zn@Pec-X). In the range of 165−340 °C, it is the decomposition of the organic structure of polysaccharides. The third loss of mass is observed between 340 and 480 °C, and it corresponds to the release of gases from the combustion of polysaccharide chains. The last loss of mass is beyond 480 °C. It can be attributed to the complete combustion of the organic phase and the beginning of the formation of zinc oxide particles. Thereafter, the oxides ZnO-Alg, ZnO-Chi, ZnO-CMC, and ZnO-Pec are stabilized at 780, 720, 790, and 840 °C, respectively. On the basis of those analysis results, 850 °C was the calcination temperature of choice for the heat treatment of all of the samples in order to remove the organic matrix (biopolymer) and release the perfectly crystallized ZnO.

*FTIR Analysis of Hybrid Beads.* FTIR analysis was performed to identify and characterize the chemical groups present in the hybrid materials, their chemical environment, as well as the nature of the bonds and the mass of the atoms involved, i.e., the chemical structure of the hybrid materials in order to understand their mechanisms of action influencing the growth of ZnO upon heat treatment.

Figure 2 shows the FTIR of xerogels prepared via chelation of $Zn^{2+}$ cations by the following four biopolymers: alginate, CMC,

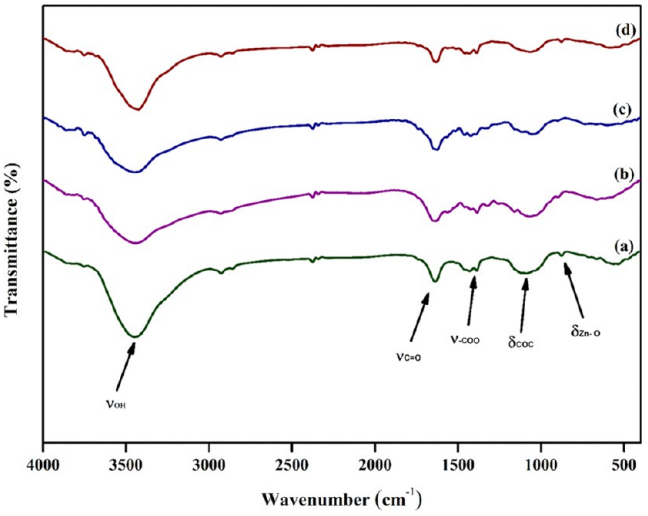


**Figure 2.** FTIR spectra of xerogels: Zn@Alg-X (a), Zn@Chi-X (b), Zn@CMC-X (c), and Zn@Pec-X (d).

pectin, and chitosan. All spectra confirmed the presence of specific bands corresponding to several functional groups, indicating that the used polysaccharides (Figure S3) act successfully as a structuring agent to control the nucleation and growth of ZnO NPs. These functional groups on biopolymers can make the nucleation/growth process easier to achieve and subsequently control the size and shape of the particles. All samples revealed that the presence of a band at 3440 $cm^{-1}$ corresponds to the stretching vibration of −OH groups characteristic of intermolecular bonded O−H, which is probably due to the interaction between ZnO NPs and hydroxyl groups of used biopolymers as a structuring agent. That at 2930 $cm^{-1}$ corresponds to the stretching vibration of C−H. The band observed at 1633 $cm^{-1}$ is related to the C═O group and that at 1430 $cm^{-1}$ corresponds to the −COO group. The presence of the band at 1068 $cm^{-1}$ is related to the stretching vibrations of C−O−C. The peak at 565 $cm^{-1}$ represents Zn−O stretching bonds, which suggested the presence of a zinc oxide phase not yet crystallized in the as-prepared xerogels. In follow-up to this analysis, all samples are composed of functional groups of biopolymers, zinc oxide, and absorbed water. All xerogels present the same vibratory modes and the same characteristic bands with a slight difference in peak intensity due to the difference in the spatial distribution and arrangement of each macromolecule (biopolymer) (Figure S3).

*Morphological Analysis of Hybrid Beads.* SEM micrographs of xerogels are shown in Figure 3. All xerogels have a spherical shape. At high magnification, SEM images of xerogel beads


https://doi.org/10.1021/acsomega.3c01491
ACS Omega 2023, 8, 24952−24963

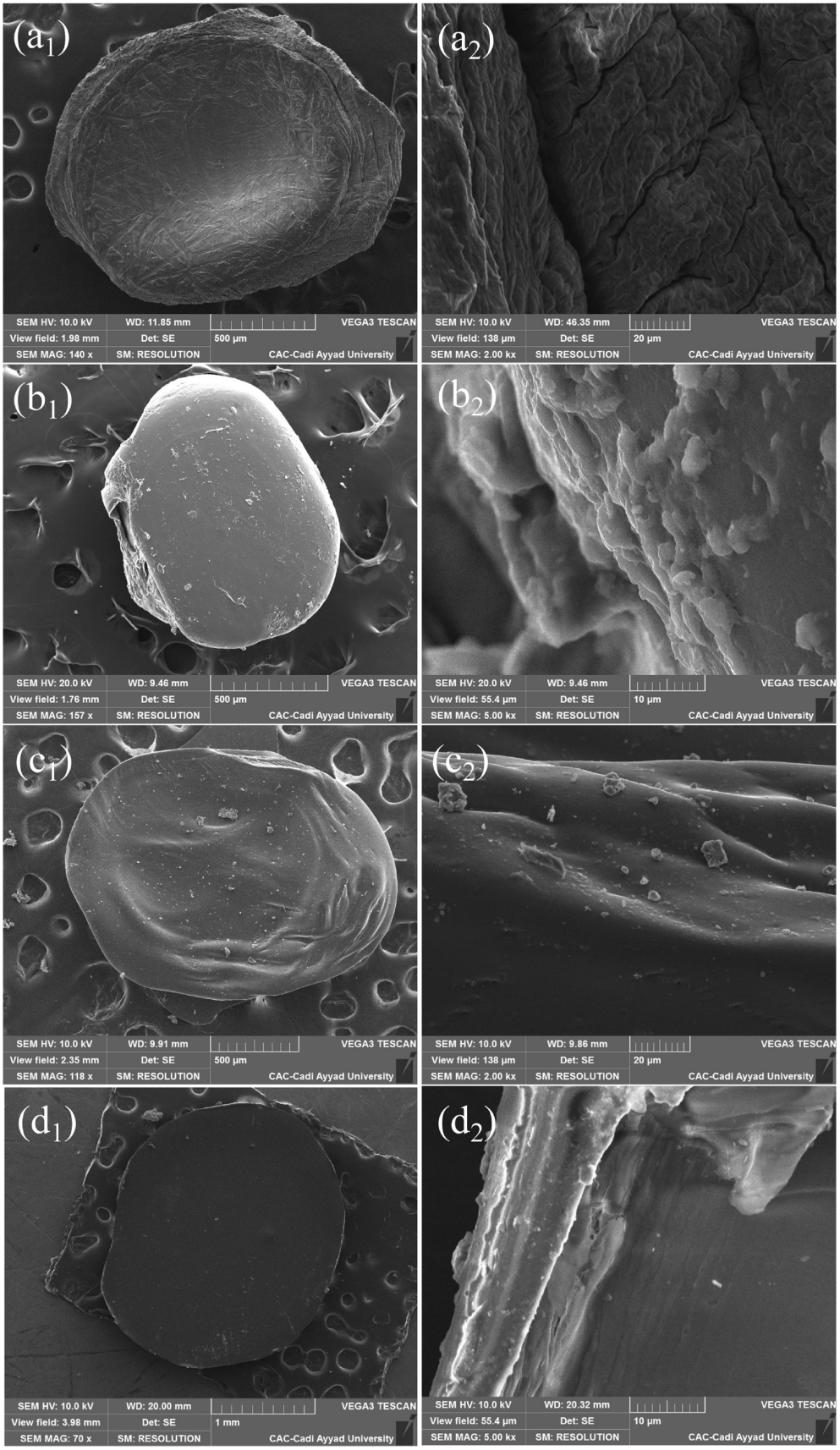


**Figure 3.** FEG-SEM images of Zn@Alg-X ($a_1$, $a_2$), Zn@Chi-X ($b_1$, $b_2$), Zn@CMC-X ($c_1$, $c_2$), and Zn@Pec-X ($d_1$, $d_2$).

synthesized using alginate show a fibrillar structure. The xerogels prepared with chitosan or CMC show a rough surface, whereas the sample synthesized via pectin has a smooth surface. Figure S4 shows the energy-dispersive spectroscopy analysis of the



https://doi.org/10.1021/acsomega.3c01491
*ACS Omega* 2023, 8, 24952−24963

hybrid beads. According to the EDS results, the xerogels are composed of carbon, oxygen, and zinc atoms. The carbon atoms are sourced from the gelling agent and confirm the formation of an organic/inorganic hybrid material, which is in line with the results of the FTIR analysis.

**Characterization of As-Prepared ZnO.** *Microstructural Analysis.* The XRD patterns of ZnO-Alg, ZnO-Chi, ZnO-CMC, and ZnO-Pec are shown in Figure 4. The observed diffraction

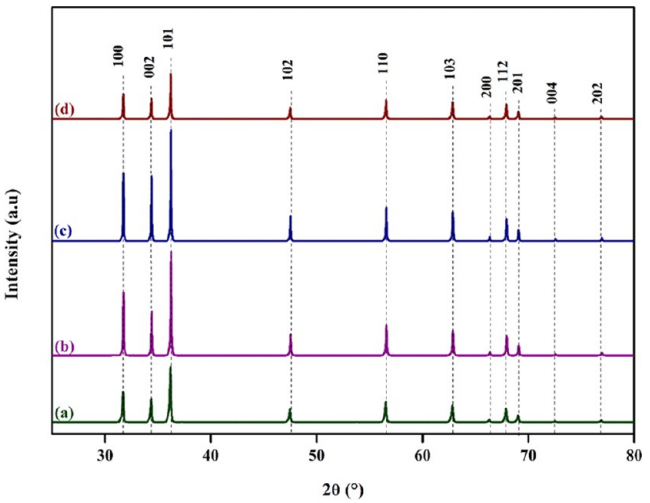


**Figure 4.** XRD patterns of the ZnO samples: ZnO-Alg (a), ZnO-Chi (b), ZnO-CMC (c), and ZnO-Pec (d).

peaks revealed the formation of a hexagonal wurtzite phase (*P*63*mc* space group (ICDD card no. 96−900−4180)). No additional peaks were observed, indicating the high purity of ZnO nanoparticles. This analysis reveals the presence of intense and narrow peaks, indicating the high crystallinity of samples. Also, intense and narrow peaks are shown at the (101) facet in the case of CMC and chitosan, which can be explained by the presence of a preferred orientation of ZnO crystallites along this facet. ZnO powders are known to be dominated by the mixed orientations of lower surface energy.[50] But in the case of thin-film ZnO, it is generally reported that ZnO grows easily in the (002) direction, which corresponds to the growth along the *c*-axis, due to the low energy of formation of this plane.[51] We also note that the semiquantitative EDS analysis reveals the purity of as-prepared ZnO (Figure S5). On the other hand, it is interesting to note that XRD patterns of all xerogels did not exhibit any diffraction peak, indicating that hybrid beads are amorphous and not yet crystallized.

The lattice parameters of the samples were calculated according to eq 1[52]

$$\frac{1}{D_{hkl}^2} = \frac{4}{3a^2} \times (h^2 + hk + k^2) + \frac{l^2}{c^2} \tag{1}$$

The bond length ($L$) of the Zn−O bond was calculated using eq 2, whereas the volume of the unit cell was calculated using eq 3[52]

$$L = \sqrt{\frac{a^2}{3} + \left(\frac{1}{2} - u\right)^2 c^2} \tag{2}$$

$$V = \frac{\sqrt{3}}{2}(a^2 c) \tag{3}$$

with

$$u = \left[\frac{1}{3}\left(\frac{a}{c}\right)^2 + 0,\ 25\right] \tag{4}$$

The calculated lattice parameters, Zn−O bond length, and lattice volume of different samples are shown in Table 2.

**Table 2. Lattice Parameters, Bond Length, and Volume Cell of the Prepared Samples of ZnO**

| | lattice parameters (Å) | | | bond length (Å) | lattice volume ($nm^3$) |
|---|---|---|---|---|---|
| samples | *a* | *b* | *c* | *L* | *V* |
| ZnO-Alg | 3.2553 | 3.2553 | 5.2128 | 1.98 | 4.78 |
| ZnO-Chi | 3.2512 | 3.2512 | 5.2076 | 1.98 | 4.76 |
| ZnO-CMC | 3.2525 | 3.2525 | 5.2091 | 1.98 | 4.77 |
| ZnO-Pec | 3.2531 | 3.2531 | 5.2106 | 1.98 | 4.77 |

The values of lattice parameters, bond length, and lattice volume are similar for all samples, regardless of the used gelling agent. The XRD peaks of ZnO-CMC and ZnO-Chi are more intense and narrower than those of ZnO-Alg and ZnO-Pec and can be related to a preferred orientation according to the facet (101), as we have already mentioned above. The crystallite size, dislocation density, and microstrain of ZnO nanoparticles were calculated using the Debye−Scherrer equations (eqs 5−7)[53]

$$D = \frac{0,\ 9\lambda}{\beta \cos\theta} \tag{5}$$

$$\delta = \frac{1}{D^2} \tag{6}$$

$$\varepsilon = \frac{\beta}{4 \tan\theta} \tag{7}$$

where $D$ is the crystallite size (nm), $\delta$ is the dislocation density ($nm^{-2}$), $\varepsilon$ is the microstrain, $\beta$ is the line broadening at the full width at half-maximum (FWHM) (radian), $\theta$ is Bragg's angle in degrees (half of $2\theta$), and $\lambda$ is the X-ray wavelength (nm), $\lambda$ (Cu K$\alpha$ = 15,406 Å).

Table 3 shows different crystallite sizes, dislocation densities, and microstrains of the as-synthesized ZnO.

**Table 3. Crystallite Size, Dislocation Density, and Microstrain as a Function of Different Biopolymers Used**

| samples | the crystallite size (nm) | dislocation density ($\times 10^{-3}\cdot nm^{-2}$) | microstrain ($\times 10^{-3}$) |
|---|---|---|---|
| ZnO-Alg | 50.76 | 0.39 | 1.21 |
| ZnO-Chi | 63.39 | 0.25 | 0.97 |
| ZnO-CMC | 69.65 | 0.21 | 0.89 |
| ZnO-Pec | 67.87 | 0.22 | 0.91 |

The ZnO-Alg crystallite size is the smallest, and this is directly related to the crystallinity of the oxide as it has the least intense and broadest diffraction peaks. In addition, it is noted that the dislocation density and the microstrain values of ZnO-CMC are the lowest, and the presence of these defects can affect the optical properties of ZnO particles. The differences in the crystallite size, dislocation density, and strain values could be related to the difference in the functional groups of monomer units in each biopolymer and the difference in their mechanism of action upon gelling. It is a very complex process due to the


https://doi.org/10.1021/acsomega.3c01491
ACS Omega 2023, 8, 24952−24963

many parameters likely to intervene in order to control the size, distribution, and shape of the particles synthesized under these given conditions.

FTIR spectra of ZnO-Alg, ZnO-Chi, ZnO-CMC, and ZnO-Pec oxides are shown in Figure 5. The intense and broad bands

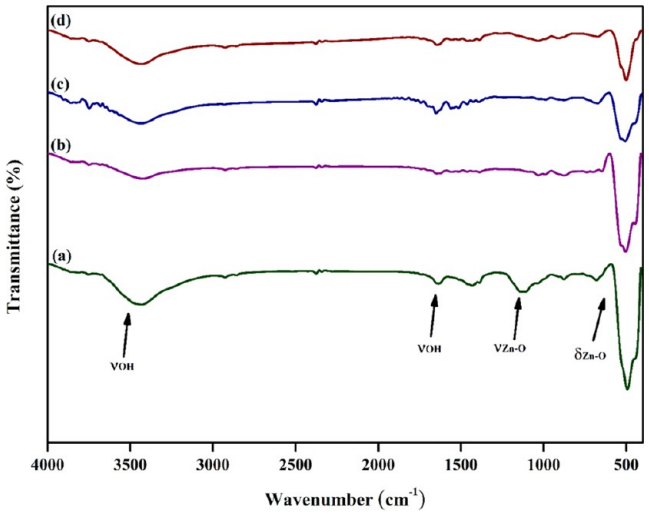


**Figure 5.** FTIR spectra of the ZnO NPs: ZnO-Alg (a), ZnO-Chi (b), ZnO-CMC (c), and ZnO-Pec (d).

around 450−600 $cm^{-1}$ in all spectra correspond to the Zn−O stretching bonds,[37] and those at 1033 $cm^{-1}$ are related to the vibrations of Zn−O. This is the fingerprint of this oxide. The other bands located at 3430 and 1460 $cm^{-1}$ corresponding to the vibrational modes of the O−H group are related to the presence of adsorbed water on oxide's surface.

The specific surface area of ZnO NPs was determined from $N_2$ adsorption/desorption isotherms data. The values obtained via the BET method are shown in Table 4. The specific surface areas

**Table 4. Surface Area Values of Photocatalysts**

| samples | ZnO-Alg | ZnO-Chi | ZnO-CMC | ZnO-Pec |
|---|---|---|---|---|
| Specific surface area ($m^2/g$) | 31.2 | 36.8 | 31.6 | 18.5 |

obtained for ZnO-Alg, ZnO-Chi, ZnO-CMC, and ZnO-Pec were 31.2, 36.8, 31.6, and 18.5 $m^2/g$, respectively. We observe, thus, that the sample prepared by using pectin had the lowest specific surface area compared to the other samples and that their specific surface areas are more or less close. It should be noted that the surface area of the oxides is strongly affected by the synthesis and postsynthesis conditions (drying mode and calcination temperature).[49]

*Morphological Analysis of Hybrid Beads.* FEG-SEM images of the ZnO NPs are shown in Figure 6. In these FEG-SEM images, we can observe the different shapes of ZnO crystallites. Thus, for the sample ZnO-Alg, the particles have a quasi-spherical shape. In the case of ZnO-Chi, the particles have a minirod shape. For ZnO-CMC, the particles have an irregular polygon shape that does not meet the regularity condition. While for the sample ZnO-Pec, the particles have a rod shape of some hundred nanometers in length. To better observe the particles, it was necessary to perform magnifications for each sample. The magnification allowed us to clearly visualize the shape of the ZnO crystallites prepared via this biopolymer gelation process as detailed above. This analysis allowed us to determine that the average particle size for the samples (ZnO-Alg, ZnO-Chi, and ZnO-CMC) is around 50 to 100 nm, and for the ZnO-Pec sample, the length is around 700 nm. EDAX results of oxides are shown in Figure S5. The oxides are mainly composed of zinc and oxygen atoms. These results confirm the findings of a high-purity zinc oxide.

**Mechanism of Gelation.** In the current study, we investigated the effect of the gelling agent used on the nanostructured zinc oxide and its photocatalytic performance. The biopolymers used are polysaccharides that can form hydrogels in the presence of $Zn^{2+}$ cations. The use of external gelation, also known as the diffusion setting method, allows cations of metal to freely diffuse into the biopolymer droplets, which provides a high strength of the formed hydrogels.[54−56] The presence of carboxyl groups in sodium alginates, CMC, and pectin allows the coordination of zinc cations to form physically cross-linked hydrogels with improved water resistance according to the "egg-box" model, whereas the formation of hydrogels via chitosan requires the gelation in two steps.[57] Egg-box models of different hydrogels are shown in Schemes S1−S4. The use of the gelation method for the elaboration of ZnO samples allowed the formation of nanostructured zinc oxide nanoparticles. The gelation mechanism of sodium alginate, chitosan, CMC, and pectin can be mainly divided into three steps: (i) the formation of monocomplexes between monomers and Zn cations; (ii) the formation of egg-box dimers by the pairing of the mono-complexes; and (iii) the formation of multimers by the lateral cross-linking of the egg-box dimers.[58] The egg-box model of sodium alginate and CMC could be described as the cross-link between a single chain of biopolymers and $Zn^{2+}$ cations and the production of regular geometric holes where cations are embedded through coordination with oxygen atoms present in the structure of biopolymers (Schemes S1 and S3); the same egg-box model could be used to describe the gelation via chitosan except that for chitosan, the cross-linking is carried out between a chain of biopolymer and $Na^+$, then in the second step, the zinc cations replace $Na^+$ (Scheme S2). On the other hand, the egg-box model of pectin is described by the cross-link between zinc cations and two antiparallel chains of pectin (Scheme S4).

According to the microstructural characterization, all biopolymers used allow formation of a pure phase of nanoparticles of zinc oxide with a wurtzite structure. This pure phase is obtained from the calcination of nanohybrids composed of polysaccharides and zinc oxides, which helps to structure the ZnO nanoparticles and to offer high porosity after the release of the organic phase. Despite the fact that all of the gelling agents used have the same gelation mechanism, the obtained zinc oxide nanoparticles have different crystallite size, surface area, and morphology, which mean that those parameters are affected by the biopolymer's properties, such as the molecular weight, the form of polymeric chains, and the source of the biopolymers. The results of physical and chemical characterization (FTIR, XRD, SEM, and EDAX-EDS) confirm that the biopolymer's nature affects the crystallite size, porosity, and morphology of ZnO nanoparticles.

The crystallite size of the obtained oxides was different: 50.76 nm for sodium alginate, 63.39 nm for chitosan, 69.65 nm for CMC, and 67.87 nm for pectin. The specific surface area values of ZnO-Alg, ZnO-Chi, ZnO-CMC, and ZnO-Pec are 31.2, 36.8, 31.6, and 18.5 $m^2/g$, respectively. The specific surface area values are in accordance with the proposed mechanism, since for pectin, we have the lowest surface area because of the low


https://doi.org/10.1021/acsomega.3c01491
ACS Omega 2023, 8, 24952−24963

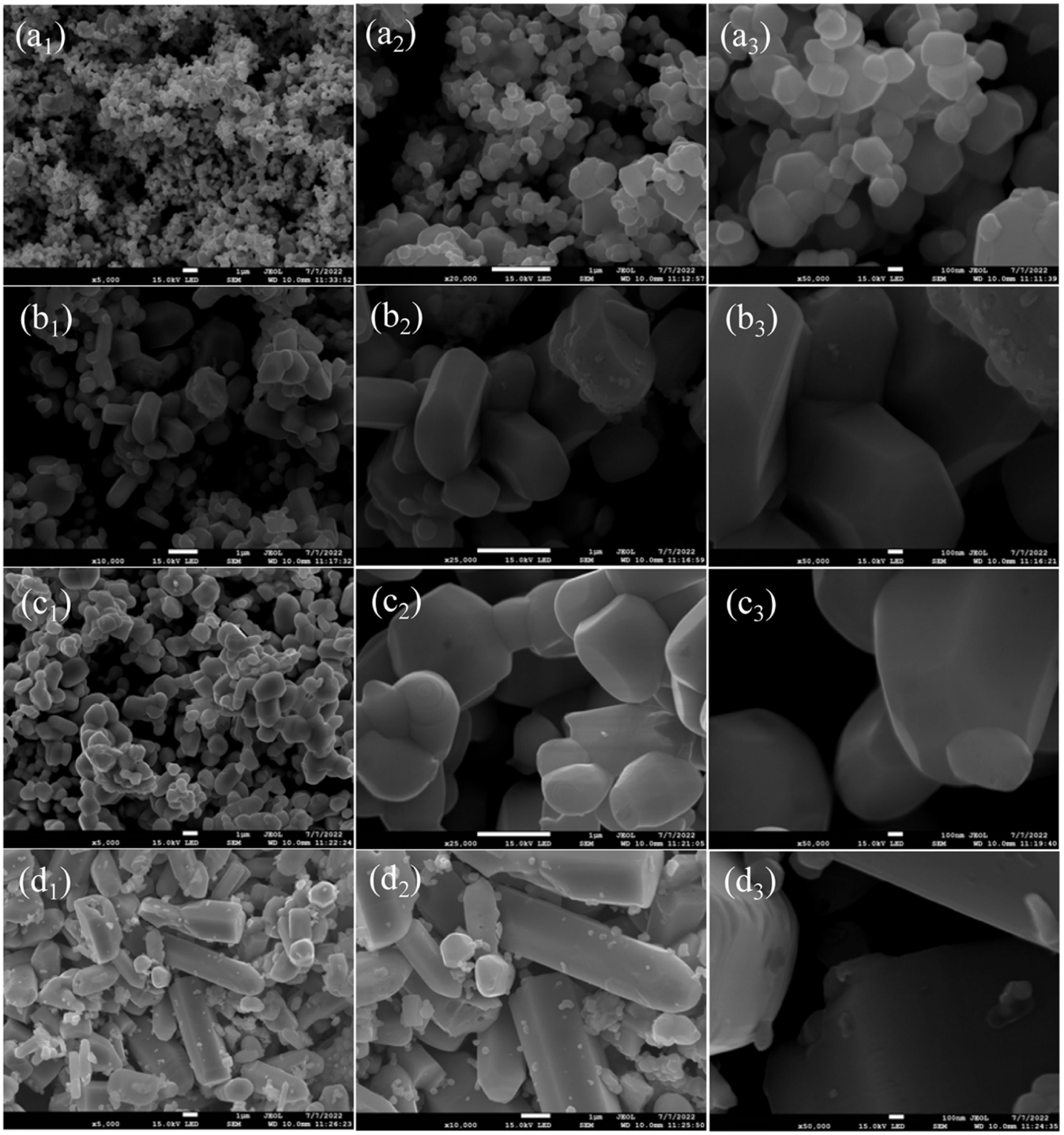


**Figure 6.** FEG-SEM images of the ZnO NPs that form during the calcination of the prepared xerogels via biopolymer gelation: ZnO-Alg ($a_1$, $a_2$, $a_3$), ZnO-Chi ($b_1$, $b_2$, $b_3$), ZnO-CMC ($c_1$, $c_2$, $c_3$), and ZnO-Pec ($d_1$, $d_2$, $d_3$).

diffusion of $Zn^{2+}$. This result is also confirmed by the morphological characterization of the elaborated xerogels. The Zn@Pec-X sample has a smooth and flattened shape related to the low diffusion of zinc cations, which leads to the formation of weak hydrogels, whereas the used sodium alginate, CMC, and chitosan give well-formed hydrogels and lead to the formation of quasi-spherical zinc nanoparticles.

The physical property of the carbohydrates used to form hydrogels helps to structure the zinc oxide and to elaborate porous nanoparticles, which enhance the photocatalytic efficiency of the elaborated zinc oxide by increasing the amount of accessible surface adsorption and reaction sites, which offers more photogenerated electrons and holes.[59,60]

The photocatalytic activity of the prepared ZnO oxides depends on several parameters, such as crystallinity, phase composition, morphology, chemical composition, particle size, electron−hole pair recombination rate, and synthesis process.

**Optical Properties of ZnO Samples.** Diffuse reflectance spectroscopy was used to analyze the optical absorption of materials[61] (Figure 7). All samples had an intense UV



https://doi.org/10.1021/acsomega.3c01491
ACS Omega 2023, 8, 24952−24963

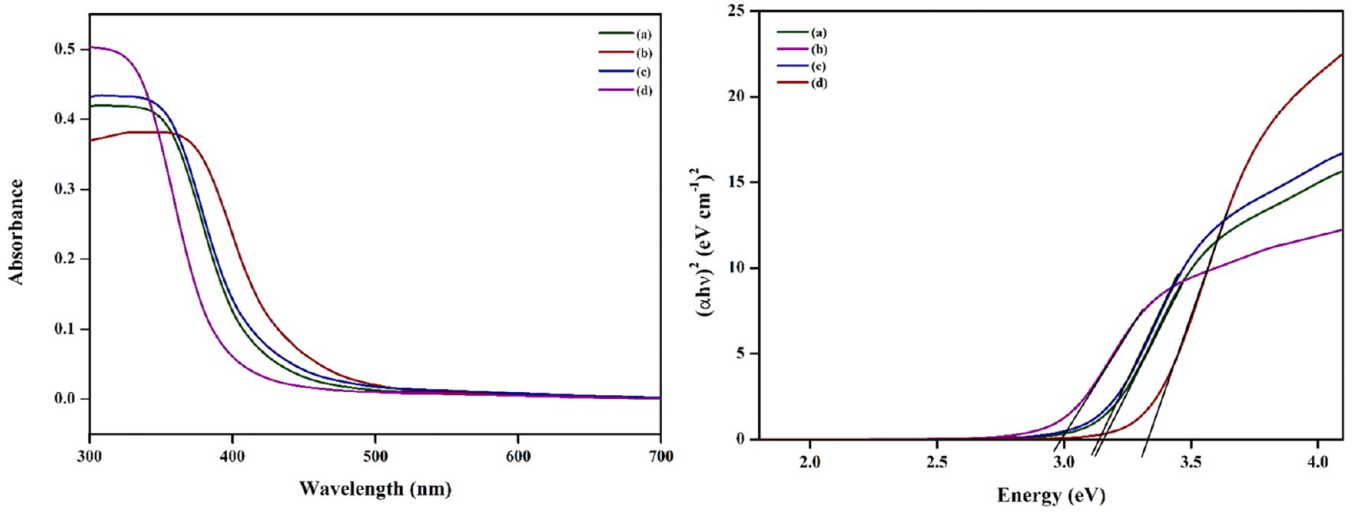


**Figure 7.** UV−vis diffuse reflectance spectroscopy of prepared ZnO nanoparticles: ZnO-Alg (a), ZnO-Chi (b), ZnO-CMC (c), and ZnO-Pec (d).

absorption with an absorption beyond 350 nm, and a shift toward the visible region was observed for ZnO-Chi. Band gap values were calculated using the Tauc plot method. The band gap values were 3.17, 2.98, 3.13, and 3.34 eV for ZnO-Alg, ZnO-Chi, ZnO-CMC, and ZnO-Pec, respectively. All samples had weaker band gap values compared to commercial ZnO (3.37 eV).[62,63] However, ZnO-Chi can harvest UV and visible light energy and release electrons/holes under UV−visible illumination, which will act as a good photocatalyst.

**Photocatalytic Properties of As-Prepared ZnO Samples.** The surface charge of oxides was measured using zeta potential. The values of zeta potential of all ZnO samples are presented in Table 5. The zeta potential values obtained are

**Table 5. ζ-Potential Values of the As-Prepared ZnO NPs**

| samples | ZnO-Alg | ZnO-Chi | ZnO-CMC | ZnO-Pec |
|---|---|---|---|---|
| ζ-potential (mV) | −15.26 | −14.46 | −23.07 | −13.17 |

−15.26, −14.46, −23.07, and −13.17 (mV) for, respectively, ZnO-Alg, ZnO-Chi, ZnO-CMC, and ZnO-Pec. The oxide prepared using CMC (ZnO-CMC) reveals the lowest ζ-potential value (−23.07 mV) compared to the other samples with approximately close values. These results led us to choose the anionic dye Orange G to overcome the adsorption phenomenon of the dye on the surface of ZnO particles due to the electrostatic repulsion between the negative charges of the ZnO surface and the dye molecules (anionic character).

The photocatalytic performance of zinc oxides is tested toward degradation of the Orange G dye in an aqueous solution at regular intervals (every 15 min). This degradation was followed by optical absorption measurement at 478 nm. To ensure the elimination of the adsorption effect, all ZnO samples were stirred in the dark for 1 h, and then the Orange G solutions were irradiated with UV radiation for 3 h in the presence of the photocatalyst. Figure 8 represents the adsorption−photcatalytic degradation activity of performed samples: ZnO-Alg, ZnO-Chi, ZnO-CMC, and ZnO-Pec. The dark adsorption percentage values of zinc oxide nanoparticles are 32.3, 21.9, 29.9, and 28.5% corresponding to ZnO-Alg, ZnO-Chi, ZnO-CMC, and ZnO-Pec, respectively. The lowest adsorption capacity was noted for ZnO-Chi.

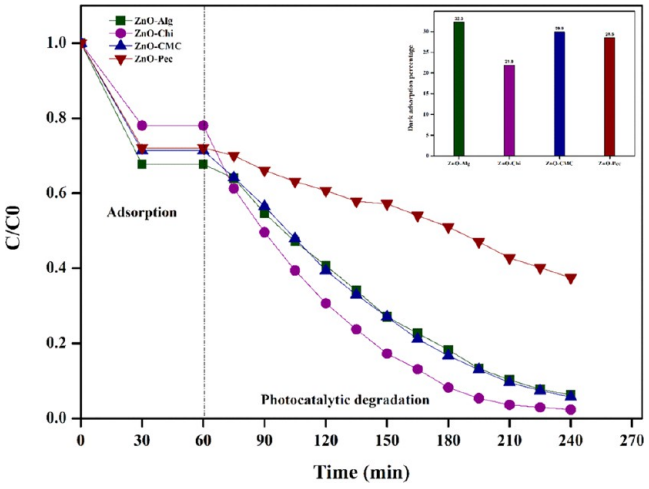


**Figure 8.** Adsorption−photocatalytic degradation activity of as-prepared ZnO nanoparticles.

The dye photodegradation tests performed for 180 min reveal that the degradation rates were 49.3, 93.2, 94.4, and 99.3% for ZnO-Pec, ZnO-Alg, ZnO-CMC, and ZnO-Chi, respectively (Table 6). ZnO-Chi has a higher degradation rate compared to

**Table 6. Kinetic Constants, Linear Regression, and Degradation Percentage of Orange G by Different Samples of the As-Prepared Zinc Oxide**

| samples | kinetic constant ($\times 10^{-2}$·min$^{-1}$) | linear regression | degradation percentage (%) |
|---|---|---|---|
| ZnO-Alg | 1.52 | 0.9711 | 93.2 |
| ZnO-Chi | 2.69 | 0.9579 | 99.3 |
| ZnO-CMC | 1.60 | 0.9754 | 94.4 |
| ZnO-Pec | 0.37 | 0.9732 | 49.3 |

the other samples. This sample presents the best photocatalytic performances, maybe due to its surface state (topography) and its defect geometry. Indeed, the surface of a material is the seat of many interactions with the environment. The physicochemical properties of the surfaces and the interfaces thus play a determining role with regard to their photocatalytic activity. Moreover, real crystals always contain a certain number of


https://doi.org/10.1021/acsomega.3c01491
ACS Omega 2023, 8, 24952−24963

defects or singularities in variable quantity. The presence and number of defects depend on the type of chemical bonding, the purity of the crystal, the preparation method, as well as the thermal and/or mechanical treatments undergone. The dislocation of the prepared samples is a linear defect (i.e., nonpunctual), corresponding to a discontinuity in the organization of the crystal structure (Table 3). We distinguish in general the wedge dislocations, the screw dislocations, and the other mixed dislocations.

The photocatalytic degradation kinetics of the Orange G dye is described by the pseudo-first-order kinetic model, which is expressed as follows[64−66]

$$-\ln\left(\frac{C}{C_0}\right) = k \times t \tag{8}$$

where $C$ is the initial concentration of Orange G, $C_0$ is the concentration of the OG dye at $t \neq 0$, $k$ is the kinetic constant, and $t$ is the time of reaction.

Figure 9 shows the line of $-\ln(C/C_0)$ versus time. The correlation coefficient $R^2$ values of ZnO-Alg, ZnO-Chi, ZnO-CMC, and ZnO-Pec are 0.9711, 0.9579, 0.9754, and 0.9732, respectively. Thus, the pseudo-first-order model perfectly fits the experimental photocatalytic study. The different values of the constant $k$ are summarized in Table 6. The kinetic constants are 0.0152, 0.0269, 0.016, and 0.0037 $min^{-1}$ corresponding to the ZnO-Alg, ZnO-Chi, ZnO-CMC, and ZnO-Pec samples, respectively.

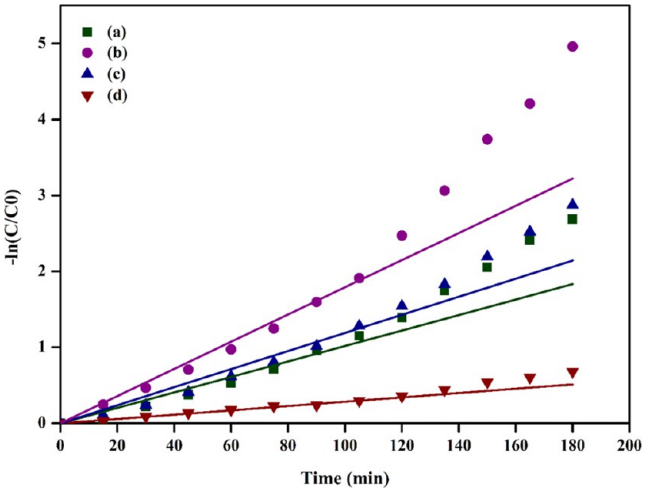


**Figure 9.** Kinetics of the Orange G degradation reaction using oxides: ZnO-Alg (a), ZnO-Chi (b), ZnO-CMC (c), and ZnO-Pec (d).

Thus, we notice that the two synthesized oxides using sodium alginate and CMC as the gelling agent have the same photocatalytic performance (93.2 and 94.4%) and the ZnO-Chi (99.3%) sample shows the best photocatalytic performance compared to other synthesized oxides. This may be due to their remarkable structural and morphological properties such as small crystallite size and high porosity. It can also be due to the large specific surface area of the ZnO-Chi sample (36.8 $m^2/g$), which favors the separation of photogenerated charge carriers for ZnO-Chi and results in more efficient catalysts. These characteristics could be related to the main function of chitosan monomer (amine $-NH_2$) and the synthesis process (gelation in two steps).

*Effect of pH.* The effect of pH on the photocatalytic degradation of Orange G (30 $\mu$M) using 1 g/L ZnO-Chi was tested (Figure 10). Excellent degradation activity was revealed at acidic and neutral conditions (pH = 4 and pH = 7). At pH = 9, lower degradation efficiency was noted for ZnO-Chi (74% of orange G degradation). These results indicate that alkali conditions limit the degradation efficiency of ZnO-Chi. At higher pH, there was an excess of $OH^-$ anions that cover the surface of the photocatalyst forming a passivation layer, which decreases the degradation efficiency of the material.

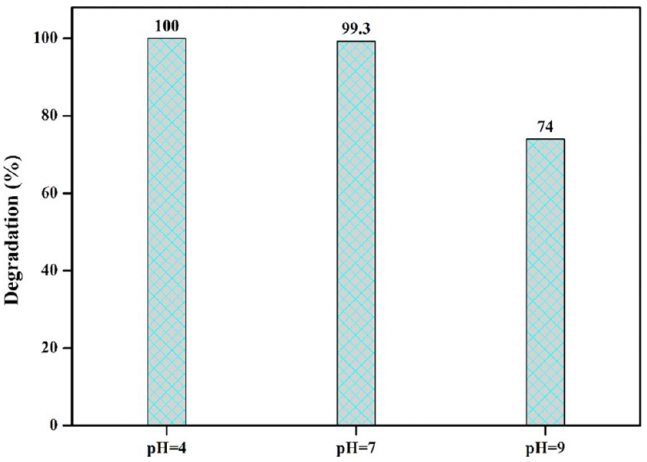


**Figure 10.** Effect of pH on the photocatalytic degradation of Orange G using ZnO-Chi (photocatalyst dosage = 1 g/L, dye concentration = 30 $\mu$M).

*Mechanism of Photodegradation.* To understand the mechanism behind photocatalysis, a series of experiments were conducted on the optimal sample, ZnO-Chi, by adding different scavengers (*t*-BuOH and EDTA). The results, shown in Figure S6, revealed that the photodegradation of orange G was not significantly affected by the addition of *t*-BuOH, a radical scavenger. However, the addition of EDTA, a hole scavenger, significantly decreased the photocatalytic activity of the hybrid, indicating that photogenerated holes are the primary oxidative species driving the photocatalytic reaction in the ZnO-Chi system.

*Reusability and Stability of the ZnO Photocatalyst.* The stability and recycling performance of ZnO-Chi were studied. After four photocatalytic degradation experiments, the degradation activities of orange G were 99.3, 97.8, 96.6, and 97.7%, respectively (Figure S7), indicating that ZnO-Chi had excellent cyclic photocatalytic degradation activity. XRD and FTIR analyses were further compared before and after photodegradation to investigate the structural stability of the sample. Obviously, the XRD patterns of the photocatalyst did not change before and after the reaction (Figure 11), indicating that it has good crystal structure stability. At the same time, the FTIR test results showed that no new characteristic peaks appeared after the photodegradation for four cycles (Figure 11). The above analysis showed that ZnO-Chi has excellent structure and photocatalytic degradation stability.

## CONCLUSIONS

In summary, we were initially interested in optimizing the process for the synthesis of ZnO nanoparticles via the gelation method of biopolymers (alginate, CMC, pectin, and chitosan). The gelation of each of the three biopolymers (alginate, CMC,


https://doi.org/10.1021/acsomega.3c01491
ACS Omega 2023, 8, 24952−24963

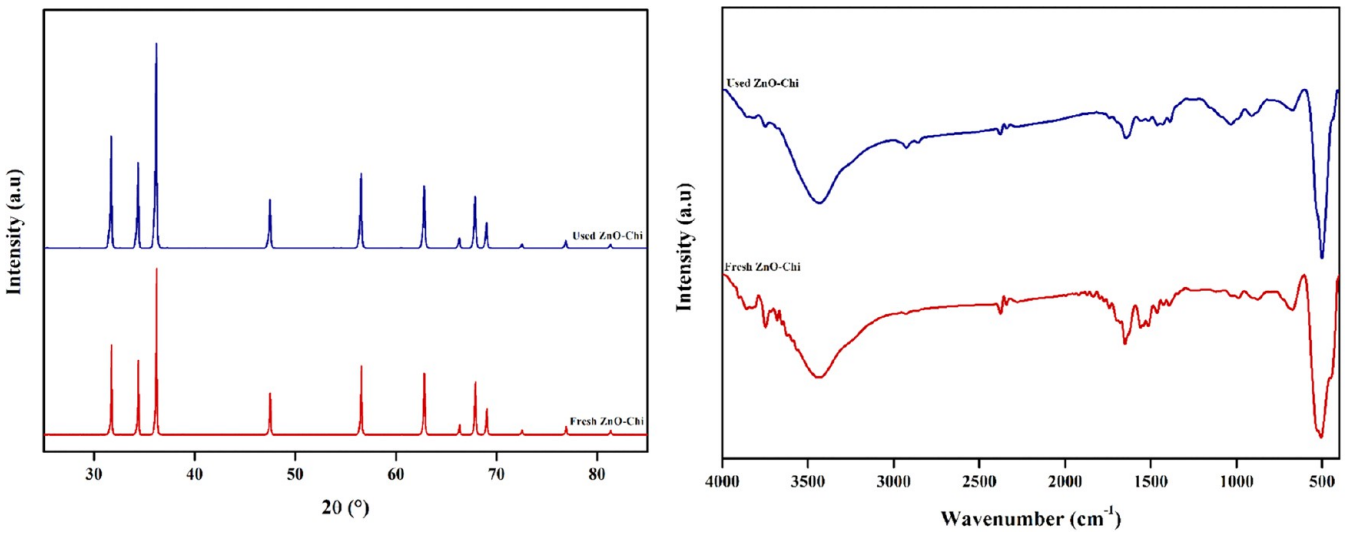


**Figure 11.** XRD and FTIR of ZnO-Chi before and after photocatalytic degradation.

pectin) was carried out via a cross-linking process by diffusion of $Zn^{2+}$ cations. The interest of such a process was based on obtaining hydrogels, whose $Zn^{2+}$ cations follow the spatial distribution of molecular forms of biopolymers. This process helps to obtain micro- and nanofibers containing ZnO nanoparticles according to the results of FTIR analysis. After calcination of the xerogels, hierarchical ZnO nanostructures with variable morphologies were obtained. A two-step process using chitosan was optimized, which helped us to obtain ZnO minirods with excellent morphological and structural properties with very good reproducibility. Thereafter, a water purification study to check whether the photocatalytic effect can be used to degrade the Orange G dye was carried out on as-prepared ZnO samples under UV irradiation. The ZnO sample prepared via pectin gelation had the lowest degradation rate, while the degradation rates for the samples prepared by using alginate, CMC, and chitosan were quantitatively similar with a slight predominance of the sample prepared by using chitosan.

## ■ ASSOCIATED CONTENT

### Supporting Information

The Supporting Information is available free of charge at https://pubs.acs.org/doi/10.1021/acsomega.3c01491.

Schematic representation of direct and two-step gelation methods; FTIR spectra of biopolymers used as the gelling agent; EDS of elaborated hybrid beads and zinc oxide nanoparticles; and mechanism of gelation using various tested biopolymers (PDF)

## ■ AUTHOR INFORMATION


### Corresponding Author

**Karima Abdelouahdi** − *IMED-Lab, FST-Marrakech, University Cadi Ayyad, 40000 Marrakech, Morocco;* orcid.org/0000-0002-1618-0427; Email: abdelouahdi@gmail.com, k.abdelouahdi@uca.ma

### Authors

**Loubna El Faroudi** − *IMED-Lab, FST-Marrakech, University Cadi Ayyad, 40000 Marrakech, Morocco*

**Latifa Saadi** − *IMED-Lab, FST-Marrakech, University Cadi Ayyad, 40000 Marrakech, Morocco*

**Abdellatif Barakat** − *IATE, Montpellier University, INRAE, Agro Institut, 34060 Montpellier, France; Mohamed VI Polytechnic University, 43150 Ben Guerir, Morocco*

**Mohammed Mansori** − *IMED-Lab, FST-Marrakech, University Cadi Ayyad, 40000 Marrakech, Morocco*

**Abderrahim Solhy** − *IATE, Montpellier University, INRAE, Agro Institut, 34060 Montpellier, France*

Complete contact information is available at: https://pubs.acs.org/10.1021/acsomega.3c01491


### Author Contributions

All authors contributed equally to this work and also to the writing of the manuscript. All authors have given approval to the final version of the manuscript.


### Funding

This work has received funding from CNRST.


### Notes

The authors declare no competing financial interest.

## ■ ACKNOWLEDGMENTS


The authors are grateful to the CNRST Research Excellence Fellowship program for financial support to LEF. They thank all of the administrative and technical support teams from CAC at Cadi Ayyad University and from UATRS at CNRST. They would also like to thank Prof. Saadoune Ismeal, former director of IMED-Lab, for his support.


## ■ REFERENCES


(1) Klingshirn, C. F.; Waag, A.; Hoffmann, A.; Geurts, J. *Zinc Oxide: From Fundamental Properties Towards Novel Applications*; Springer Science & Business Media, 2010.

(2) Huang, J.; Yin, Z.; Zheng, Q. Applications of ZnO in Organic and Hybrid Solar Cells. *Energy Environ. Sci.* **2011**, *4*, 3861−3877.

(3) Bhati, V. S.; Hojamberdiev, M.; Kumar, M. Enhanced Sensing Performance of ZnO Nanostructures-Based Gas Sensors: A Review. *Energy Rep.* **2020**, *6*, 46−62.

(4) Mirzaeifard, Z.; Shariatinia, Z.; Jourshabani, M.; Darvishi, S. M. R. ZnO Photocatalyst Revisited: Effective Photocatalytic Degradation of Emerging Contaminants Using S-Doped ZnO Nanoparticles under Visible Light Radiation. *Ind. Eng. Chem. Res.* **2020**, *59*, 15894−15911.

(5) Qin, X.; Xu, H.; Zhang, G.; Wang, J.; Wang, Z.; Zhao, Y.; Wang, Z.; Tan, T.; Bockstaller, M. R.; Zhang, L.; Matyjaszewski, K. Enhancing the




https://doi.org/10.1021/acsomega.3c01491
*ACS Omega* 2023, 8, 24952−24963

Performance of Rubber with Nano ZnO as Activators. *ACS Appl. Mater. Interfaces* **2020**, *12*, 48007−48015.
(6) de Lucas-Gil, E.; Menéndez, J.; Pascual, L.; Fernández, J. F.; Rubio-Marcos, F. The Benefits of the ZnO/Clay Composite Formation as a Promising Antifungal Coating for Paint Applications. *Appl. Sci.* **2020**, *10*, No. 1322.
(7) Swain, P. S.; Rao, S. B. N.; Rajendran, D.; Dominic, G.; Selvaraju, S. Nano Zinc, an Alternative to Conventional Zinc as Animal Feed Supplement: A Review. *Anim. Nutr.* **2016**, *2*, 134−141.
(8) Prasad, A. R.; Williams, L.; Garvasis, J.; Shamsheera, K. O.; Basheer, S. M.; Kuruvilla, M.; Joseph, A. Applications of Phytogenic ZnO Nanoparticles: A Review on Recent Advancements. *J. Mol. Liq.* **2021**, *331*, No. 115805.
(9) Raha, S.; Ahmaruzzaman, M. ZnO Nanostructured Materials and Their Potential Applications: Progress, Challenges and Perspectives. *Nanoscale Adv.* **2022**, *4*, 1868−1925.
(10) Singh, T. A.; Das, J.; Sil, P. C. Zinc Oxide Nanoparticles: A Comprehensive Review on Its Synthesis, Anticancer and Drug Delivery Applications as Well as Health Risks. *Adv. Colloid Interface Sci.* **2020**, *286*, No. 102317.
(11) Skorenko, K.; Bernier, R. T.; Liu, J.; Galusha, B.; Goroleski, F.; Hughes, B. P.; Bernier, W. E.; Jones, W. E. Thermal Stability of ZnO Nanoparticle Bound Organic Chromophores. *Dyes Pigm.* **2016**, *131*, 69−75.
(12) Heinonen, S.; Nikkanen, J.-P.; Huttunen-Saarivirta, E.; Levänen, E. Investigation of Long-Term Chemical Stability of Structured ZnO Films in Aqueous Solutions of Varying Conditions. *Thin Solid Films* **2017**, *638*, 410−419.
(13) Zhou, J.; Xu, N. S.; Wang, Z. L. Dissolving Behavior and Stability of ZnO Wires in Biofluids: A Study on Biodegradability and Biocompatibility of ZnO Nanostructures. *Adv. Mater.* **2006**, *18*, 2432−2435.
(14) Lee, K. M.; Lai, C. W.; Ngai, K. S.; Juan, J. C. Recent Developments of Zinc Oxide Based Photocatalyst in Water Treatment Technology: A Review. *Water Res.* **2016**, *88*, 428−448.
(15) Sahoo, D.; Mandal, A.; Mitra, T.; Chakraborty, K.; Bardhan, M.; Dasgupta, A. K. Nanosensing of Pesticides by Zinc Oxide Quantum Dot: An Optical and Electrochemical Approach for the Detection of Pesticides in Water. *J. Agric. Food Chem.* **2018**, *66*, 414−423.
(16) Subramanian, H.; Krishnan, M.; Mahalingam, A. Photocatalytic Dye Degradation and Photoexcited Anti-Microbial Activities of Green Zinc Oxide Nanoparticles Synthesized via Sargassum Muticum Extracts. *RSC Adv.* **2021**, *12*, 985−997.
(17) Behnajady, M. A.; Modirshahla, N.; Hamzavi, R. Kinetic Study on Photocatalytic Degradation of C.I. Acid Yellow 23 by ZnO Photocatalyst. *J. Hazard. Mater.* **2006**, *133*, 226−232.
(18) Coulibaly, G. N.; Bae, S.; Kim, J.; Assadi, A. A.; Hanna, K. Enhanced Removal of Antibiotics in Hospital Wastewater by Fe−ZnO Activated Persulfate Oxidation. *Environ. Sci.: Water Res. Technol.* **2019**, *5*, 2193−2201.
(19) Postica, V.; Vahl, A.; Santos-Carballal, D.; Dankwort, T.; Kienle, L.; Hoppe, M.; Cadi-Essadek, A.; de Leeuw, N. H.; Terasa, M.-I.; Adelung, R.; Faupel, F.; Lupan, O. Tuning ZnO Sensors Reactivity toward Volatile Organic Compounds via Ag Doping and Nanoparticle Functionalization. *ACS Appl. Mater. Interfaces* **2019**, *11*, 31452−31466.
(20) Dimapilis, E. A. S.; Hsu, C.-S.; Mendoza, R. M. O.; Lu, M.-C. Zinc Oxide Nanoparticles for Water Disinfection. *Sustainable Environ. Res.* **2018**, *28*, 47−56.
(21) Gunalan, S.; Sivaraj, R.; Rajendran, V. Green Synthesized ZnO Nanoparticles against Bacterial and Fungal Pathogens. *Prog. Nat. Sci.: Mater. Int.* **2012**, *22*, 693−700.
(22) Madihi-Bidgoli, S.; Asadnezhad, S.; Yaghoot-Nezhad, A.; Hassani, A. Azurobine Degradation Using Fe2O3@multi-Walled Carbon Nanotube Activated Peroxymonosulfate (PMS) under UVA-LED Irradiation: Performance, Mechanism and Environmental Application. *J. Environ. Chem. Eng.* **2021**, *9*, No. 106660.
(23) Kaur, Y.; Chopra, L. In *Natural Dyes - An Eco-Friendly Approach to Textile Industry*, AIP Conference Proceedings; AIP Publishing, 2023.
(24) Al-Tohamy, R.; Ali, S. S.; Li, F.; Okasha, K. M.; Mahmoud, Y. A.-G.; Elsamahy, T.; Jiao, H.; Fu, Y.; Sun, J. A Critical Review on the Treatment of Dye-Containing Wastewater: Ecotoxicological and Health Concerns of Textile Dyes and Possible Remediation Approaches for Environmental Safety. *Ecotoxicol. Environ. Saf.* **2022**, *231*, No. 113160.
(25) Hassani, A.; Eghbali, P.; Mahdipour, F.; Wacławek, S.; Lin, K.-Y. A.; Ghanbari, F. Insights into the Synergistic Role of Photocatalytic Activation of Peroxymonosulfate by UVA-LED Irradiation over CoFe2O4-RGO Nanocomposite towards Effective Bisphenol A Degradation: Performance, Mineralization, and Activation Mechanism. *Chem. Eng. J.* **2023**, *453*, No. 139556.
(26) Hassani, A.; Krishnan, S.; Scaria, J.; Eghbali, P.; Nidheesh, P. V. Z-Scheme Photocatalysts for Visible-Light-Driven Pollutants Degradation: A Review on Recent Advancements. *Curr. Opin. Solid State Mater. Sci.* **2021**, *25*, No. 100941.
(27) Abebe, B.; Murthy, H. C. A.; Amare, E. Enhancing the Photocatalytic Efficiency of ZnO: Defects, Heterojunction, and Optimization. *Environ. Nanotechnol., Monit. Manage.* **2020**, *14*, No. 100336.
(28) Giraldi, T. R.; Santos, G. V. F.; de Mendonca, V. R.; Ribeiro, C.; Weber, I. T. Effect of Synthesis Parameters on the Structural Characteristics and Photocatalytic Activity of ZnO. *Mater. Chem. Phys.* **2012**, *136*, 505−511.
(29) Mclaren, A.; Valdes-Solis, T.; Li, G.; Tsang, S. C. Shape and Size Effects of ZnO Nanocrystals on Photocatalytic Activity. *J. Am. Chem. Soc.* **2009**, *131*, 12540−12541.
(30) Ayoub, I.; Kumar, V.; Abolhassani, R.; Sehgal, R.; Sharma, V.; Sehgal, R.; Swart, H. C.; Mishra, Y. K. Advances in ZnO: Manipulation of Defects for Enhancing Their Technological Potentials. *Nanotechnol. Rev.* **2022**, *11*, 575−619.
(31) Han, Z.; Ren, L.; Cui, Z.; Chen, C.; Pan, H.; Chen, J. Ag/ZnO Flower Heterostructures as a Visible-Light Driven Photocatalyst via Surface Plasmon Resonance. *Appl. Catal., B* **2012**, *126*, 298−305.
(32) Djurišić, A. B.; Chen, X.; Leung, Y. H.; Ng, A. M. C. ZnO Nanostructures: Growth, Properties and Applications. *J. Mater. Chem.* **2012**, *22*, 6526−6535.
(33) Hasnidawani, J. N.; Azlina, H. N.; Norita, H.; Bonnia, N. N.; Ratim, S.; Ali, E. S. Synthesis of ZnO Nanostructures Using Sol-Gel Method. *Procedia Chem.* **2016**, *19*, 211−216.
(34) Adam, R. E.; Pozina, G.; Willander, M.; Nur, O. Synthesis of ZnO Nanoparticles by Co-Precipitation Method for Solar Driven Photodegradation of Congo Red Dye at Different PH. *Photonics Nanostruct. - Fundam. Appl.* **2018**, *32*, 11−18.
(35) Maryanti, E.; Damayanti, D.; Gustian, I.; Yudha, S. S. Synthesis of ZnO Nanoparticles by Hydrothermal Method in Aqueous Rinds Extracts of Sapindus Rarak DC. *Mater. Lett.* **2014**, *118*, 96−98.
(36) Hassani, A.; Faraji, M.; Eghbali, P. Facile Fabrication of Mpg-C3N4/Ag/ZnO Nanowires/Zn Photocatalyst Plates for Photodegradation of Dye Pollutant. *J. Photochem. Photobiol., A* **2020**, *400*, No. 112665.
(37) Velmurugan, R.; Selvam, K.; Krishnakumar, B.; Swaminathan, M. An Efficient Reusable and Antiphotocorrosive Nano ZnO for the Mineralization of Reactive Orange 4 under UV-A Light. *Sep. Purif. Technol.* **2011**, *80*, 119−124.
(38) Akhtar, K.; Zubair, N.; Ikram, S.; Khan, Z. U.; Khalid, H. Synthesis and Characterization of ZnO Nanostructures with Varying Morphology. *Bull. Mater. Sci.* **2017**, *40*, 459−466.
(39) Shaba, E. Y.; Jacob, J. O.; Tijani, J. O.; Suleiman, M. A. T. A Critical Review of Synthesis Parameters Affecting the Properties of Zinc Oxide Nanoparticle and Its Application in Wastewater Treatment. *Appl. Water Sci.* **2021**, *11*, No. 48.
(40) Ramananarivo, H. R.; Maati, H.; Amadine, O.; Abdelouahdi, K.; Barakat, A.; Ihiawakrim, D.; Ersen, O.; Varma, R. S.; Solhy, A. Ecofriendly Synthesis of Ceria Foam via Carboxymethylcellulose Gelation: Application for the Epoxidation of Chalcone. *ACS Sustainable Chem. Eng.* **2015**, *3*, 2786−2795.
(41) Suba, S.; Vijayakumar, S.; Vidhya, E.; Punitha, V. N.; Nilavukkarasi, M. Microbial Mediated Synthesis of ZnO Nanoparticles


https://doi.org/10.1021/acsomega.3c01491
*ACS Omega* 2023, 8, 24952−24963

Derived from Lactobacillus Spp: Characterizations, Antimicrobial and Biocompatibility Efficiencies. *Sens. Int.* **2021**, *2*, No. 100104.
(42) Mohd Yusof, H.; Abdul Rahman, N.; Mohamad, R.; Zaidan, U. H.; Samsudin, A. A. Biosynthesis of Zinc Oxide Nanoparticles by Cell-Biomass and Supernatant of Lactobacillus Plantarum TA4 and Its Antibacterial and Biocompatibility Properties. *Sci. Rep.* **2020**, *10*, No. 19996.
(43) Shamim, A.; Mahmood, T.; Abid, M. B. Biogenic Synthesis of Zinc Oxide (ZnO) Nanoparticles Using a Fungus (*Aspargillus Niger*) and Their Characterization. *Int. J. Chem.* **2019**, *11*, No. 119.
(44) Consolo, V. F.; Torres-Nicolini, A.; Alvarez, V. A. Mycosinthetized Ag, CuO and ZnO Nanoparticles from a Promising Trichoderma Harzianum Strain and Their Antifungal Potential against Important Phytopathogens. *Sci. Rep.* **2020**, *10*, No. 20499.
(45) Ebadi, M.; Zolfaghari, M. R.; Aghaei, S. S.; Zargar, M.; Shafiei, M.; Zahiri, H. S.; Noghabi, K. A. A Bio-Inspired Strategy for the Synthesis of Zinc Oxide Nanoparticles (ZnO NPs) Using the Cell Extract of Cyanobacterium Nostoc Sp. EA03: From Biological Function to Toxicity Evaluation. *RSC Adv.* **2019**, *9*, 23508−23525.
(46) Ramesh, P.; Saravanan, K.; Manogar, P.; Johnson, J.; Vinoth, E.; Mayakannan, M. Green Synthesis and Characterization of Biocompatible Zinc Oxide Nanoparticles and Evaluation of Its Antibacterial Potential. *Sens. Bio-Sens. Res.* **2021**, *31*, No. 100399.
(47) Hamrayev, H.; Shameli, K. Biopolymer-Based Green Synthesis of Zinc Oxide (ZnO) Nanoparticles. *IOP Conf. Ser.: Mater. Sci. Eng.* **2021**, *1051*, No. 012088.
(48) Ramananarivo, H. R.; Abdelouahdi, K.; Amer, W.; Zahouily, M.; Clark, J.; Solhy, A. Tunable Structure of Zirconia Nanoparticles by Biopolymer Gelation: Design, Synthesis and Characterization. *Eur. J. Inorg. Chem.* **2012**, *2012*, 5465−5469.
(49) El Jemli, Y.; Mansori, M.; Diaz, O. G.; Barakat, A.; Solhy, A.; Abdelouahdi, K. Controlling the Growth of Nanosized Titania via Polymer Gelation for Photocatalytic Applications. *RSC Adv.* **2020**, *10*, 19443−19453.
(50) Meyer, B.; Marx, D. Density-Functional Study of the Structure and Stability of ZnO Surfaces. *Phys. Rev. B* **2003**, *67*, No. 035403.
(51) Lokhande, B. J.; Patil, P. S.; Uplane, M. D. Deposition of Highly Oriented ZnO Films by Spray Pyrolysis and Their Structural, Optical and Electrical Characterization. *Mater. Lett.* **2002**, *57*, 573−579.
(52) Samanta, P. K. Band Gap Engineering, Quantum Confinement, Defect Mediated Broadband Visible Photoluminescence and Associated Quantum States of Size Tuned Zinc Oxide Nanostructures. *Optik* **2020**, *221*, No. 165337.
(53) Rao, S. M. A.; Kotteeswaran, S.; Visagamani, A. M. Green Synthesis of Zinc Oxide Nanoparticles from Camellia Sinensis: Organic Dye Degradation and Antibacterial Activity. *Inorg. Chem. Commun.* **2021**, *134*, No. 108956.
(54) Lin, D.; Kelly, A. L.; Maidannyk, V.; Miao, S. Effect of Concentrations of Alginate, Soy Protein Isolate and Sunflower Oil on Water Loss, Shrinkage, Elastic and Structural Properties of Alginate-Based Emulsion Gel Beads during Gelation. *Food Hydrocolloids* **2020**, *108*, No. 105998.
(55) Lee, B.-B.; Bhandari, B. R.; Howes, T. Gelation of an Alginate Film via Spraying of Calcium Chloride Droplets. *Chem. Eng. Sci.* **2018**, *183*, 1−12.
(56) Liu, Y.; Tottori, N.; Nisisako, T. Microfluidic Synthesis of Highly Spherical Calcium Alginate Hydrogels Based on External Gelation Using an Emulsion Reactant. *Sens. Actuators, B* **2019**, *283*, 802−809.
(57) Cao, L.; Lu, W.; Mata, A.; Nishinari, K.; Fang, Y. Egg-Box Model-Based Gelation of Alginate and Pectin: A Review. *Carbohydr. Polym.* **2020**, *242*, No. 116389.
(58) Wang, H.; Fei, S.; Wang, Y.; Zan, L.; Zhu, J. Comparative Study on the Self-Assembly of Pectin and Alginate Molecules Regulated by Calcium Ions Investigated by Atomic Force Microscopy. *Carbohydr. Polym.* **2020**, *231*, No. 115673.
(59) Sangon, S.; Hunt, A. J.; Ngernyen, Y.; Youngme, S.; Supanchaiyamat, N. Rice Straw-Derived Highly Mesoporous Carbon-Zinc Oxide Nanocomposites as High Performance Photocatalytic Adsorbents for Toxic Dyes. *J. Cleaner Prod.* **2021**, *318*, No. 128583.
(60) Abarna, B.; Preethi, T.; Karunanithi, A.; Rajarajeswari, G. R. Influence of Jute Template on the Surface, Optical and Photocatalytic Properties of Sol-Gel Derived Mesoporous Zinc Oxide. *Mater. Sci. Semicond. Process.* **2016**, *56*, 243−250.
(61) Yaghoot-Nezhad, A.; Wacławek, S.; Madihi-Bidgoli, S.; Hassani, A.; Lin, K.-Y. A.; Ghanbari, F. Heterogeneous Photocatalytic Activation of Electrogenerated Chlorine for the Production of Reactive Oxygen and Chlorine Species: A New Approach for Bisphenol A Degradation in Saline Wastewater. *J. Hazard. Mater.* **2023**, *445*, No. 130626.
(62) Madathil, A. N. P.; Vanaja, K. A.; Jayaraj, M. K. Synthesis of ZnO Nanoparticles by Hydrothermal Method. In *Nanophotonic Materials IV*; SPIE, 2007; Vol. *6639*, pp 47−55.
(63) Jain, A.; Sagar, P.; Mehra, R. M. Band Gap Widening and Narrowing in Moderately and Heavily Doped N-ZnO Films. *Solid-State Electron.* **2006**, *50*, 1420−1424.
(64) Zhang, S.; Lin, T.; Chen, W.; Xu, H.; Tao, H. Degradation Kinetics, Byproducts Formation and Estimated Toxicity of Metronidazole (MNZ) during Chlor(Am)Ination. *Chemosphere* **2019**, *235*, 21−31.
(65) Hu, C.-Y.; Hou, Y.-Z.; Lin, Y.-L.; Li, A.-P.; Deng, Y.-G. Degradation Kinetics of Diatrizoate during UV Photolysis and UV/Chlorination. *Chem. Eng. J.* **2019**, *360*, 1003−1010.
(66) Mohammadi, A.; Khadir, A.; Tehrani, R. M. A. Optimization of Nitrogen Removal from an Anaerobic Digester Effluent by Electrocoagulation Process. *J. Environ. Chem. Eng.* **2019**, *7*, No. 103195.


https://doi.org/10.1021/acsomega.3c01491
*ACS Omega* 2023, 8, 24952−24963